OPEN ACCESS

University of BRISTOL

Champneys, A. R., van der Heijden, G. H. M., & Thompson, J. M. T. (1997). Spatially complex localisation after one-twist-per-wave equilibrium in twisted circular rods with initial curvature.

Early version, also known as pre-print

Link to publication record in Explore Bristol Research
PDF-document

Spatially complex localisation after one-twist-per-wave equilibria in twisted circular rods with initial curvature

A.R. Champneys,[*] G.H.M. van der Heijden[†] & J.M.T. Thompson[†]

Abstract

In experiments on long rubber rods subject to end tension and moment, a one-twist-per-wave deformation is often observed on the fundamental path prior to the onset of localised buckling. An analysis is undertaken here to account for this observed behaviour. First we derive general equilibrium equations using the Cosserat theory, incorporating the effects of non-symmetric cross section, shear deformation, gravity, and a uniform initial curvature of the unstressed rod. Each of these effects in turn can be expressed as a perturbation of the classical completely integrable Kirchhoff-Love differential equations which are equivalent to those describing a spinning symmetric top. Non-symmetric cross-section was dealt with in earlier papers. Here, after demonstrating that shear deformation alone makes little qualitative difference, the case of initial curvature is examined in some detail.

It is shown that the straight configuration of the rod is replaced by a one-twist-per wave equilibrium whose amplitude varies with pre-buckling load. Superimposed on this equilibrium is a localised buckling mode, which can be described as a homoclinic orbit to the new fundamental path. The dependence is measured of the pre-buckled state and critical buckling load on the amount of initial curvature. Numerical techniques are used to explore the multiplicity of localised buckling modes, given that non-zero initial curvature breaks the complete integrability of the differential equations, and also one of a pair of reversibilities.

Finally, the physical implications of the results are assessed and are shown to match qualitatively what is observed in an experiment.

1   Introduction

The torsional buckling of long rods subject to end moment and tension is a fundamental problem, with applications to DNA supercoiling and pipeline, cable and optical fibre kinking (see Thompson & Champneys (1996) and references therein). The mathematical modelling of such phenomena has a long history, going at least as far back as Kirchhoff (1859). See Antman

---

[*]Department of Engineering Mathematics, University of Bristol, University Walk, Bristol BS8 1TR, UK.
[†]Centre for Nonlinear Dynamics, University College London, Gower Street, London WC1E 6BT, UK.

(1995, Ch. VIII) and references therein for a modern account. In earlier work (Thompson & Champneys 1996, Champneys & Thompson 1996, van der Heijden, Champneys & Thompson 1996, van der Heijden & Thompson 1996) we considered the nature of buckling of a long, initially straight rod with uniform cross-section subject to end moment M and tension T. Experiments and energy analysis suggested that a localised form of deformation was the preferred mode of buckling at the critical buckling load. This buckling load, for a perfect, inextensible rod with symmetric cross-section, is given by the simple dimensionless condition

$$m = m_c = 2, \qquad \text{where} \qquad m := M/\sqrt{BT}, \tag{1}$$

and B is the bending stiffness (Timoshenko & Gere 1961, Eq. 2-74).

For moderately large deflection (so that the buckled rod does not have a non-trivial contact with itself) the spatial equilibrium of a rod is described (with one caveat, see below) by the Kirchhoff-Love, or more generally the Cosserat, theory of rods (see Section 2 below for the details). Here the rod is described by arclength along its center line and three directors which are aligned along the rod's principal axes of inertia. This leads to a system of ordinary differential equations for the contact forces and moments in the arclength-dependent co-ordinate basis described by the directors. It was (Kirchhoff 1859) who noticed that the equilibrium equations for infinitely long symmetric rods have identical form to the classical completely integrable system describing the dynamics of a symmetric spinning top. At the buckling load, the differential equations undergo a Hamiltonian-Hopf bifurcation (van der Meer 1985, Iooss & Pérouème 1993), included in the normal form of which is a homoclinic solution. This solution represents a localised helical deformation that tends asymptotically to the flat, unbuckled equilibrium state of the rod. That the two end states must be physically aligned was not made clear in our previous work, but is a subtle property of the structure of the underlying equations; see Kehrbaum & Maddocks (1997) in this issue.

The situation is more complex, however, for rods without circular cross-section – more precisely for rods whose principal bending stiffness about two orthogonal planes are not equal – because the complete integrability of the differential equations is broken. For mildly anisotropic rods, this leads to spatial chaos in the differential equations and, more importantly to the problem of interest here, to an infinite multiplicity of multi-modal localised buckling paths (Mielke & Holmes 1988, Champneys & Thompson 1996, van der Heijden et al. 1996) existing right up to the buckling state. For strongly anisotropic rods with certain physical properties (sufficiently low Poisson's ratio, for example), a transition occurs to different buckling behaviour, with localised buckling being 'locked-on to tape-like behaviour' (van der Heijden & Thompson 1996), and multi-modal solutions only existing in a region of parameter space bounded away from the buckling state.

Qualitative experiments on circular and square cross-section rubber rods reported in Champneys & Thompson (1996) agree well with the theory, but with one caveat; see Thompson & Champneys (1996, Figs. 4 & 6) and also Figs. 12 and 13 in Section 5 below. Prior to buckling a marked spatially-periodic helical deformation is observed, on top of which at the critical load the localised buckling mode is superimposed. The characteristics of the observed pre-buckled and post-buckled helical deformations are quite distinct. The pre-buckled state has one twist per wave whereas the buckling mode has approximately three twists per wave.

The aim of this paper is to analyse an effect that is responsible for such a pre-buckled one-twist-per-wave deformation. Effects missing from our earlier analysis were, the effect of gravity

(most experiments were carried out with the specimen held horizontally, often seen to hang in a shallow catenary); shear deformation (the rod was assumed to be inextensible and transversely unshearable in the analysis – inextensibility is clearly violated for the observations made under rigid loading); and initial curvature of the rod in its unstressed state (a permanent deformation caused by the fact that most specimens are stored in loosely-wound coils). It is interesting to note the observation mentioned briefly in Thompson & Champneys (1996, Section 6) that the one-twist-per-wave mode was not observed in neutral-buoyancy under-water tests on rubber rods that had been cast in a rectangular trough and hence had no initial curvature.

The rest of the paper is outlined as follows. In Section 2, we review the Cosserat theory of rods applied to the current problem and use it to derive non-dimensional equilibrium equations for infinite rods subject to shear deformation and gravity, and having initial curvature and not necessarily symmetric cross-section. Each of these four effects can be treated as perturbations of the underlying 'perfect' problem. Our programme of work is to treat each perturbation separately. Non-symmetric cross-section was treated in earlier work and gravity will be left for future work. The main thrust of the present work will be to treat initial curvature.

In Section 3 we review the unperturbed problem and use it to explain the numerical methods which will be used in the following. Also in Section 3, the introduction of shear deformation alone is shown to make little difference to what is observed.

Section 4 contains the analysis of the effects of initial curvature. First, it is shown that the fundamental, flat state is replaced by a new spatially-homogeneous state in the arc-length-dependent co-ordinates. It is then shown explicitly that this state has one twist per wave when interpreted physically and the amplitude and end-shortening associated with it are computed as a function of the strength of initial curvature κ_0. Next, a linearisation about this state reveals the new critical buckling load, replacing (1) as a function, $m(\kappa_0)$, of the initial curvature. Finally, numerical methods are used to compute localised buckling modes superimposed on the one-twist-per-wave equilibria. Initial curvature, like non-symmetric cross-section, is again demonstrated to imply an infinity of post-buckling modes.

Section 5 draws conclusions and considers some physical implications of the results. We also present some experimental results. These confirm the finding of this paper, that a circular rod with initial curvature, when twisted, does indeed form one-twist-per-wave pre-buckling equilibria in which bending is in the direction of the unstressed curvature.

2   Equilibrium equations

2.1   The Cosserat theory

Consider the formulation of equilibrium equations for a rod that can undergo flexure, tension, extension and shear as elucidated in Antman (1995, Ch. VIII). We are interested in the case of an infinite rod, so we begin by choosing an origin for an arclength co-ordinate s and define $\boldsymbol{r}(s)$ to be the position vector of the centre line of the rod with respect to a fixed Cartesian co-ordinate system with basis vectors $\{\boldsymbol{i}, \boldsymbol{j}, \boldsymbol{k}\}$. The configuration of the rod in a deformed state is then defined by $\boldsymbol{r}(s)$, and two orthonormal vectors $\boldsymbol{d}_1(s)$ and $\boldsymbol{d}_2(s)$ which define the position of two orthogonal lines in the cross section of the rod at s. In the case where the rod is straight and prismatic when unstrained with its centre line aligned along the z-axis, then we

3

may regard $\boldsymbol{d}_{1,2}(s)$ as defining the deformed position of the material originally aligned along the x and y axes respectively. Upon setting

$$\boldsymbol{d}_3 := \boldsymbol{d}_1 \times \boldsymbol{d}_2$$

the triple $\{\boldsymbol{d}_1(s), \boldsymbol{d}_2(s), \boldsymbol{d}_3(s)\}$ defines a moving rod-centred co-ordinate system, called the *directors* of the rod. Note that in the presence of shear, in general $\boldsymbol{d}_3(s) \neq \boldsymbol{r}'(s)$, where the prime denotes differentiation with respect to arclength. Henceforth all vectors are expressed with respect to the moving basis $\{\boldsymbol{d}_1, \boldsymbol{d}_2, \boldsymbol{d}_3\}$, unless otherwise stated.

The *stress* in the rod is defined by

$$\boldsymbol{n}(s) = n_1 \boldsymbol{d}_1 + n_2 \boldsymbol{d}_2 + n_3 \boldsymbol{d}_3 \qquad \text{and} \qquad \boldsymbol{m}(s) = m_1 \boldsymbol{d}_1 + m_2 \boldsymbol{d}_2 + m_3 \boldsymbol{d}_3,$$

which are respectively the contact force and couple exerted by the material parametrised by $\tilde{s} < s$ on that parametrised by $\tilde{s} > s$. Here $n_{1,2}$ are shear forces, n_3 is tension, $m_{1,2}$ are bending moments about the axes $\boldsymbol{d}_{1,2}$ and m_3 is the twisting moment about $\boldsymbol{d}_3$.

The *strain* of the rod is defined by two vectors

$$\boldsymbol{u}(s) = u_1 \boldsymbol{d}_1 + u_2 \boldsymbol{d}_2 + u_3 \boldsymbol{d}_3 \qquad \text{and} \qquad \boldsymbol{v}(s) = v_1 \boldsymbol{d}_1 + v_2 \boldsymbol{d}_2 + v_3 \boldsymbol{d}_3$$

defined by

$$\boldsymbol{d}_i' = \boldsymbol{u} \times \boldsymbol{d}_i, \quad i = 1, 2, 3, \qquad \text{and} \qquad \boldsymbol{r}' = \boldsymbol{v}. \tag{2}$$

Here, u_1 and u_2 measure the flexure, u_3 measures torsion, v_1 and v_2 measure transverse shear and v_3 measures dilation, or axial extension. Note that if the rod were unshearable and inextensible, then $\boldsymbol{v} = \boldsymbol{d}_3$. It is thus reasonable to redefine the shear vector as

$$\boldsymbol{v} = \boldsymbol{d}_3 + \boldsymbol{y}$$

(cf. Antman (1995, Eq. (VIII.15.13))), where $\boldsymbol{y}$ is small in a sense to be made precise in the non-dimensionalisation to follow.

Balancing forces and moments leads to the following equilibrium equations

$$\frac{\mathrm{d}\boldsymbol{n}}{\mathrm{d}s} + \boldsymbol{f} = 0, \tag{3}$$

$$\frac{\mathrm{d}\boldsymbol{m}}{\mathrm{d}s} + \boldsymbol{r}' \times \boldsymbol{n} + \boldsymbol{l} = 0, \tag{4}$$

where $\mathbf{f}$ and $\mathbf{l}$ are distributed external forces and couples acting on the rod along its length. The only body force or couple we shall be interested in will be gravity. To that end we assume in (3) and (4) that

$$\boldsymbol{l} = \boldsymbol{0} \qquad \text{and} \qquad \boldsymbol{f} = -Dg\boldsymbol{k}, \tag{5}$$

where D is the density (per unit original arclength) of the cross-section and g is the acceleration due to gravity. Note that (5) assumes that the $\boldsymbol{k}$ axis points vertically upwards.

The differentials on the left-hand side of (3) and (4) represent the total derivative with respect to arclength which is related to the derivative with respect to s in the moving co-ordinate

4

frame (which is denoted by a $'$) with the addition of terms which describe the derivative of the co-ordinate frame with respect to s. For example,

$$
\begin{aligned}
\frac{\mathrm{d}\boldsymbol{n}}{\mathrm{d}s} &= \frac{\mathrm{d}}{\mathrm{d}s}(n_1\boldsymbol{d}_1 + n_2\boldsymbol{d}_2 + n_3\boldsymbol{d}_3) \\
&= (n_1'\boldsymbol{d}_1 + n_2'\boldsymbol{d}_2 + n_3'\boldsymbol{d}_3) + (n_1\boldsymbol{d}_1' + n_2\boldsymbol{d}_2' + n_3\boldsymbol{d}_3') \\
&= \boldsymbol{n}' + (n_1\boldsymbol{u}\times\boldsymbol{d}_1 + n_2\boldsymbol{u}\times\boldsymbol{d}_2 + n_3\boldsymbol{u}\times\boldsymbol{d}_3), \qquad \text{(by (2))} \\
&= \boldsymbol{n}' + \boldsymbol{u}\times\boldsymbol{n}.
\end{aligned}
$$

Hence, using (2) and (5), (3) and (4) become

$$
\begin{aligned}
\boldsymbol{n}' &= \boldsymbol{n}\times\boldsymbol{u} + Dg\boldsymbol{k}, && (6) \\
\boldsymbol{m}' &= \boldsymbol{m}\times\boldsymbol{u} + \boldsymbol{n}\times\boldsymbol{v}. && (7)
\end{aligned}
$$

2.2 Constitutive relations and boundary conditions

It remains to specify the curvatures $\boldsymbol{u}$ and shears $\boldsymbol{v}$ in terms of the contact forces $\boldsymbol{n}$ and couples $\boldsymbol{m}$. These constitutive relations may take a quite general form (Antman 1995, Eq. (2.2)), but here we shall take the simplest linear constitutive relations allowing for the effects of initial curvature. There is evidence to suggest (Antman & Jordan 1974, Champneys & Thompson 1996) that physically realistic nonlinear constitutive laws make little qualitative difference to localised buckling. Specifically, we assume relations of the form

$$
\begin{aligned}
u_1(s) = u_0 + m_1(s)/A, \qquad u_2(s) = m_2(s)/B, \qquad u_3(s) = m_3(s)/C, \\
y_1(s) = n_1(s)/H, \qquad y_2(s) = n_2(s)/J, \qquad y_3(s) = n_3(s)/K.
\end{aligned} \qquad (8)
$$

Here, A and B are the principal bending stiffnesses about $\boldsymbol{d}_1$ and $\boldsymbol{d}_2$, C is the torsional stiffness of the rod and u_0 is an assumed initial curvature of the rod, which without loss of generality we assume to occur about the $\boldsymbol{d}_1$ axis. H and J are the transverse shear stiffnesses, and K is the axial stiffness.

Using (8) and (5) it is now possible to express (6) and (7) as a six-dimensional system of ordinary differential equations for $\boldsymbol{m}(s)$ and $\boldsymbol{n}(s)$. In order to solve this system, we must discuss its boundary conditions. In this work it is assumed that the rod is held with boundary conditions at infinity which supply a constant twisting moment M and tension T. For the time being, we consider these loads as fixed (either pre-fixed or control) parameters. In interpretation of solutions, however, one should allow for the possibility of rigid loading in which either or both of M or T are regarded as free parameters under controlled end rotation or end shortening. The boundary conditions for $\boldsymbol{n}$ and $\boldsymbol{m}$ must then satisfy

$$
\sqrt{\boldsymbol{n}.\boldsymbol{n}} \to T \quad \text{as} \quad s \to \pm\infty, \qquad \sqrt{\boldsymbol{m}.\boldsymbol{m}} \to M \quad \text{as} \quad s \to \pm\infty. \qquad (9)
$$

Note that we do not put any constraint on the directions in which $\boldsymbol{n}$ and $\boldsymbol{m}$ are pointing. These will follow from the analysis.

2.3 Non-dimensionalisation and dynamical system formulation

Equations (6) and (7) can be made dimensionless by setting

$$x_1 = n_1/T, \qquad x_2 = n_2/T, \qquad x_3 = n_3/T,$$
$$x_4 = m_1/M, \qquad x_5 = m_2/M, \qquad x_6 = m_3/M, \tag{10}$$

rescaling the axial length

$$t = \frac{M}{B} s, \tag{11}$$

and introducing the dimensionless parameters

$$m = M/\sqrt{BT}, \qquad \rho = (B/A) - 1, \qquad \nu = (B/C) - 1, \qquad \kappa_0 = Au_0/M,$$
$$\sigma = (J/H) - 1, \qquad \gamma = (J/K) - 1, \qquad \epsilon = T/J, \qquad \delta = DgB/(MT). \tag{12}$$

The parameter m is a single dimensionless load parameter, showing the equivalence (under dead loading) of increasing moment and reducing tension. ρ may be regarded as measuring the non-circularity of the cross-section of the rod. More precisely, $\rho = 0$ corresponds to the bending stiffnesses about the two principal axes being equal, which could also represent a square cross-section, for example. The parameter $\nu + 1$ measures the ratio of torsional stiffness to the greater principal bending stiffness (here we assume $B \geq A$ and hence $\rho \geq 0$). For solid rods with circular cross-section ν is equal to Poisson's ratio, with a typical physical value being $\nu = 1/3$. For rods with anisotropic cross-section, however, it should be pointed out that ν no longer equals Poisson's ratio which is given by a certain combination of ν and ρ, depending on the geometry (van der Heijden & Thompson 1996). κ_0 is the dimensionless initial curvature, and σ and γ are the analogues of ρ and ν for the shear and extension coefficients. ϵ measures the relative importance of shear compared with bending and δ measures the relative strength of gravity compared with the applied loads.

Typically we think of ϵ, δ and κ_0 as small whereas $\rho + 1$, $\nu + 1$, $\sigma + 1$ and $\gamma + 1$ are all $\mathcal{O}(1)$. It is also reasonable to set $\rho = \sigma$, with both parameters measuring the degree of non-circularity of the cross-section.

Under the non-dimensionalisation (10), (11) and (12), the equilibrium equations (6) and (7) become

$$\begin{aligned}
\dot{x}_1 &= (1 + \nu)\, x_2\, x_6 - x_3\, x_5 + \delta k_1(t) \\
\dot{x}_2 &= (1 + \rho)\, x_3\, (x_4 + \kappa_0) - (1 + \nu) x_1\, x_6 + \delta k_2(t) \\
\dot{x}_3 &= x_1\, x_5 - (1 + \rho)\, x_2\, (x_4 + \kappa_0) + \delta k_3(t) \\
\dot{x}_4 &= \nu\, x_5\, x_6 + (1/m^2)[x_2 + \epsilon\gamma\, x_2\, x_3] \\
\dot{x}_5 &= (1 + \rho)\,(x_4 + \kappa_0)\, x_6 - (1 + \nu)\, x_4\, x_6 + (1/m^2)[\epsilon\,(\sigma - \gamma)\, x_1\, x_3 - x_1] \\
\dot{x}_6 &= x_4\, x_5 - (1 + \rho)\,(x_4 + \kappa_0)\, x_5 - (\epsilon/m^2)\, \sigma\, x_1\, x_2,
\end{aligned} \tag{13}$$

where (k_1, k_2, k_3) are the components of $\boldsymbol{k}$ with respect to $\{\boldsymbol{d}_1, \boldsymbol{d}_2, \boldsymbol{d}_3\}$, and a dot denotes differentiation with respect to the scaled arclength t.

In the gravity-free case, $\delta = 0$ and (13), when regarded as an initial-value problem, represents an autonomous six-dimensional dynamical system

$$\dot{\boldsymbol{x}} = \boldsymbol{f}(\boldsymbol{x}, \lambda), \qquad \boldsymbol{x} \in \mathbb{R}^6, \qquad \lambda \in \mathbb{R}^p,$$

with p the number of parameters considered to be controlled. It can be shown to be Hamiltonian with two independent integrals of the motion (Mielke & Holmes 1988). We are interested in solutions which are localised to some portion of the axial length. Hence we apply the homoclinic boundary conditions

$$\boldsymbol{x}(t) \to \boldsymbol{x}^* \quad \text{as} \quad t \to \pm\infty, \tag{14}$$

where $\boldsymbol{x}^*$ is a spatially-homogeneous equilibrium position of the rod, that is $\boldsymbol{f}(\boldsymbol{x}^*, \lambda) = 0$, which is subject to the constraint imposed by the dimensionless version of (9),

$$\sqrt{x_1^{*2} + x_2^{*2} + x_3^{*2}} = 1, \qquad \sqrt{x_4^{*2} + x_5^{*2} + x_6^{*2}} = 1. \tag{15}$$

In order to interpret solutions to (13), (14) as configurations of the rod in physical co-ordinates, the twelve-dimensional system (2) must be solved for the $\boldsymbol{i}$, $\boldsymbol{j}$ and $\boldsymbol{k}$ components of each $\boldsymbol{d}_i$ and $\boldsymbol{r}$. The first nine of these equations are the Frenet-Serret equations of differential geometry. The dimensionless versions of (2) are

$$\dot{\boldsymbol{d}}_i = \tilde{\boldsymbol{u}} \times \boldsymbol{d}_i, \quad i = 1, 2, 3, \qquad \text{and} \qquad \dot{\tilde{\boldsymbol{r}}} = \tilde{\boldsymbol{v}}, \tag{16}$$

in which

$$\tilde{\boldsymbol{u}} = (1 + \rho)(x_4 + \kappa_0)\, \boldsymbol{d}_1 + x_5\, \boldsymbol{d}_2 + (1 + \nu)x_6\, \boldsymbol{d}_3,$$
$$\tilde{\boldsymbol{v}} = \epsilon(1 + \sigma)x_1\, \boldsymbol{d}_1 + \epsilon x_2\, \boldsymbol{d}_2 + (1 + \epsilon(1 + \gamma)x_3)\, \boldsymbol{d}_3, \qquad \tilde{\boldsymbol{r}} = (M/B)\, \boldsymbol{r}.$$

These equations can be solved after a solution to (13) has been found. $\boldsymbol{r}$ and $\boldsymbol{d}_i$ are typically subject to initial conditions specifying the position and orientation of the rod at its left-hand endpoint, $t = -\infty$.

If gravity effects are included, then $\delta \neq 0$ and (13) can no longer be regarded in isolation, but must be solved in tandem with the equations for $\boldsymbol{d}_i$ in (16) in order to calculate $\boldsymbol{k}(t)$. Notice that $\boldsymbol{k}$ is obtained from the solution of (16) by forming the matrix

$$B = (\boldsymbol{d}_1 | \boldsymbol{d}_2 | \boldsymbol{d}_3)$$

and taking

$$\boldsymbol{k} = B^{-1}(0, 0, 1)^T.$$

We may consider each of the parameters ρ ($= \sigma$), ϵ, κ_0, δ as measuring the strength of perturbations to the 'perfect', symmetric, unshearable, initially straight rod in the absence of gravity. The case of non-symmetric rods, with $\epsilon = \delta = \kappa_0 = 0$, $\rho \neq 0$, was analysed in depth in Champneys & Thompson (1996), van der Heijden et al. (1996) and van der Heijden & Thompson (1996) to which we refer the reader for the details. For the rest of this paper we shall consider only rods with symmetric cross-section $\rho = \sigma = 0$. Also, we shall not here analyse the effects of gravity, that is we set $\delta = 0$. The following section reviews the unperturbed case and then considers the effect of axial-extensibility and transverse shear ($\epsilon \neq 0$). The bulk of our analysis, in Section 4, will be for a rod with curvature when unstrained ($\kappa_0 \neq 0$) with the other perturbations fixed at zero.

3 The unperturbed case

Consider (13) for $\rho = \epsilon = \kappa_0 = \delta = 0$. First, observe that the unperturbed system (and, indeed, the wider class of systems with $\rho \neq 0$) is invariant under the following two involutions:

$$R_1: \quad (x_1, x_2, x_3, x_4, x_5, x_6) \to (-x_1, x_2, x_3, -x_4, x_5, x_6), \quad t \to -t, \tag{17}$$

$$R_2: \quad (x_1, x_2, x_3, x_4, x_5, x_6) \to (x_1, -x_2, x_3, x_4, -x_5, x_6), \quad t \to -t. \tag{18}$$

This will have implications for the multiplicity of homoclinic solutions. Next, the unperturbed system (13) is completely integrable with the following three independent 'constants of the motion':

$$I_1 := x_1^2 + x_2^2 + x_3^2 = \text{const.}, \tag{19}$$

$$I_2 := x_1 x_4 + x_2 x_5 + x_3 x_6 = \text{const.}, \tag{20}$$

$$I_3 := x_6 = \text{const.} \tag{21}$$

The integrals (19) and (20) correspond to the conservation along the axial length of the rod of the magnitude of force and the component of torque about the loading axis, respectively. (21) describes conservation of torque about the body (i.e., symmetry) axis of the rod. (Actually, the twisted rod equations are completely integrable for a much wider class of constitutive relations; see Antman (1995).)

Note that for given m, the only spatially-homogeneous equilibrium solutions of (13) that satisfy the constraint (15) are $\boldsymbol{x} = (0, 0, \pm 1, 0, 0, \pm 1)$. We can ignore the solutions with minus signs because we are considering tension rather than compression and by convention of the direction in which we apply end moment. Therefore, we set

$$\boldsymbol{x}^* = (0, 0, 1, 0, 0, 1). \tag{22}$$

Linearising about this equilibrium one finds that there are two zero eigenvalues corresponding to translations in the directions of $\boldsymbol{m}$ and $\boldsymbol{n}$. Imposing (15), in effect, fixes this translation and, through (22), the values of the integrals (19), (20), (21) for the spatially-homogeneous solution and its localised deformations. Examining the other four eigenvalues, the trivial equilibrium loses physical stability (four complex eigenvalues coalesce on the imaginary axis) as m is increased through the critical value $m = 2$. Here a Hamiltonian-Hopf bifurcation occurs (van der Meer 1985, Iooss & Pérouème 1993).

As a result of complete integrability, at the Hamiltonian-Hopf point we have the subcritical bifurcation of a manifold of localised buckling modes. Each solution in the manifold consists of a rigid rotation of a primary localised helix, that is a homoclinic solution of (13). The physical stability of these localised buckling modes under rigid loading was investigated in Thompson & Champneys (1996).

3.1 Measuring twist

Before proceeding, let us first demonstrate how the Frenet-Serret and centre line differential equations (16) may be used to give the degree of twist about the central axis for a particular physical configuration. Specifically we demonstrate that when interpreted in dimensional coordinates, the trivial equilibrium (22) corresponds to a straight rod with the tension T and

moment M being carried along the centre line of the rod. Taking $\boldsymbol{x} = \boldsymbol{x}^*$ given by (22), we find that (16) gives

$$\dot{\boldsymbol{d}}_3 = 0, \qquad \ddot{\boldsymbol{d}}_1 = -(1+\nu)^2 \boldsymbol{d}_1, \qquad \dot{\tilde{\boldsymbol{r}}} = \text{const.} \tag{23}$$

Choosing initial conditions so that $\boldsymbol{d}_3 = \boldsymbol{i}$ is horizontal, and hence

$$\tilde{\boldsymbol{r}} = t\,\boldsymbol{i}, \tag{24}$$

the second equation of (23) gives a rotation of the material of the rod about the horizontal with angular frequency (fundamental twist) $1 + \nu$.

In contrast, the wavelength of the helical deformation at the critical buckling load can be obtained by linearising about the the trivial solution at $m = 2$ (van der Heijden & Thompson 1996). This analysis uses a description of the rod in terms of Euler angles $\theta(s)$, $\psi(s)$ and $\phi(s)$ (see Love (1927, art. 253) for the definition of the angles defined using this notation). Along the trivial solution we have $\dot{\phi} = \frac{1}{2} + \nu$ while at buckling (i.e., $\theta = 0$), $\dot{\phi} + \dot{\psi} = \tau = 1 + \nu$. Hence, $\dot{\psi} = \frac{1}{2}$. Now, ψ is the azimuthal angle determining the wavelength of the helix. The number of twists per wave (tpw) can therefore be obtained as

$$\text{tpw} = \frac{\tau}{\dot{\psi}} = 2(1 + \nu). \tag{25}$$

For rubber rods ($\nu \approx 0.5$) this gives the three twists per wave observed in experiments mentioned in the Introduction (see also Section 5 below).

3.2 Numerical methods

Let us briefly outline how the numerical methods used in Champneys & Thompson (1996) and van der Heijden et al. (1996) can be adapted for the present setting. For homoclinic orbits to a fixed point we use the shooting method developed in Champneys & Spence (1993). Load-deflection-type bifurcation diagrams are subsequently obtained by continuation of these orbits as parameters are varied using the code AUTO (Doedel, Keller & Kernévez 1991) for continuation of solutions to boundary-value problems.

This combined use of shooting and continuation is robust and was described in detail in earlier papers (e.g., van der Heijden et al. (1996)) to which the reader is referred for the details. We remark, however, that these methods typically truncate the problem to an approximation of half the rod ($t \in [0, \mathcal{T}]$, $\mathcal{T}$ large), and only find solutions which are invariant under the reversibilities R_1 or R_2. Non-symmetric homoclinic orbits may also be found with more effort, by shooting over an approximation to the full length of the rod ($t \in [-\mathcal{T}, \mathcal{T}]$).

In order to compute load-deflection diagrams for localised buckling modes it is necessary to also measure the end displacement D and end rotation R from the spatially-homogeneous reference position. Once a well-posed solution to (13) has been found, we solve (16) subject to the initial conditions

$$\tilde{\boldsymbol{r}}(0) = (0,0,0), \qquad \boldsymbol{d}_1(0) = (1,0,0), \qquad \boldsymbol{d}_2(0) = (0,1,0), \qquad \boldsymbol{d}_3(0) = (0,0,1). \tag{26}$$

The end displacement and end rotation can then be obtained as

$$D = \mathcal{T} - \tilde{r}_3(\mathcal{T}), \qquad \cos R = <\boldsymbol{d}_1(\mathcal{T}),(1,0,0)>, \qquad \sin R = <\boldsymbol{d}_1(\mathcal{T}),(0,1,0)>, \tag{27}$$

9

provided $\boldsymbol{d}_3(\mathcal{T})$ is sufficiently aligned with the initial direction $\boldsymbol{d}_3(0) = (0, 0, 1)$. Although this alignment is not assured at the symmetric section, it is, for localised solutions, at the end points of the rod. Therefore, in applying (27) $\mathcal{T}$ is taken to be the full length of the rod. (The case that end vectors do not line up because the fundamental configuration of the rod is not a straight one, as happens when the rod has initial curvature, can be easily accommodated; see Section 4.3.) In (26) and (27) vectors are expressed with respect to the fixed frame $\{\boldsymbol{i}, \boldsymbol{j}, \boldsymbol{k}\}$. Note that the angle R is only defined modulo 2π in (27). Continuity with respect to the arclength parameter t, however, will allow us to keep track of the number of full turns made by the end point.

3.3 The effect of shear and extension

In this section we demonstrate that including the effect of shear alone makes little qualitative difference. To that end we take $\epsilon > 0$ in (13) while keeping $\rho = \sigma = \delta = \kappa_0 = 0$. First note that, as for the unperturbed equation, the only spatially-homogeneous equilibrium that satisfies the constraint (15) is the trivial solution (22). Setting $\boldsymbol{x} = \boldsymbol{x}^* + \boldsymbol{z}$, one obtains

$$
\begin{aligned}
\dot{z}_1 &= (1 + \nu)\, z_2\, (1 + z_6) - (1 + z_3)\, z_5 \\
\dot{z}_2 &= (1 + z_3)\, z_4 - (1 + \nu) z_1\, (1 + z_6) \\
\dot{z}_3 &= z_1\, z_5 - z_2\, z_4 \\
\dot{z}_4 &= \nu\, z_5\, (1 + z_6) + (1/m^2)[z_2 + \epsilon\gamma\, z_2\, (1 + z_3)] \\
\dot{z}_5 &= -\nu\, z_4 (1 + z_6) + (1/m^2)[-\epsilon\,\gamma\, z_1\, (1 + z_3) - z_1] \\
\dot{z}_6 &= 0.
\end{aligned}
\tag{28}
$$

Here we note that the linear terms of (28) are identical to those when $\epsilon = 0$ provided $1/m^2$ is replaced by $(1 + \epsilon\gamma)/m^2$. Hence we conclude that the local bifurcation behaviour is qualitatively identical to that in the shear-free case, with the critical buckling condition now given by

$$
m_c = 2\sqrt{1 + \gamma\epsilon}.
\tag{29}
$$

Using (12) to write this in terms of the original parameters we get

$$
\frac{M}{\sqrt{BT}} = 2\sqrt{1 + T(K^{-1} - H^{-1})},
\tag{30}
$$

where $H^{-1}(= J^{-1})$ and K^{-1} are the shear and axial flexibility, respectively. We conclude that compared with the unperturbed case ($H^{-1} = 0, K^{-1} = 0$), shear flexibility tends to lower the critical buckling load m_c, while axial flexibility tends to raise m_c.

Fig. 1 shows examples of three-dimensional rod shapes for two different values of the load m. The solutions were computed on a truncated interval using the shooting method explained in Section 4, followed by an integration of the centre line equations in (16).

Load-deflection characteristics of the localised buckling mode are given in Fig. 2. The diagrams were computed by monitoring end displacement D and end rotation R while numerically continuing the homoclinic orbit for varying m. Plotted are actually the corrected quantities $\tilde{D}$ and $\tilde{R}$ obtained from D and R by subtracting the trivial contributions, proportional to the length of the rod, which the straight unbuckled rod would have, and dividing the angle by 2π:

$$
\tilde{D} = (1 + \epsilon(1 + \gamma))\, \mathcal{T} - \tilde{r}_3(\mathcal{T}), \qquad\qquad \tilde{R} = \frac{R - (1 + \nu)\, \mathcal{T}}{2\pi},
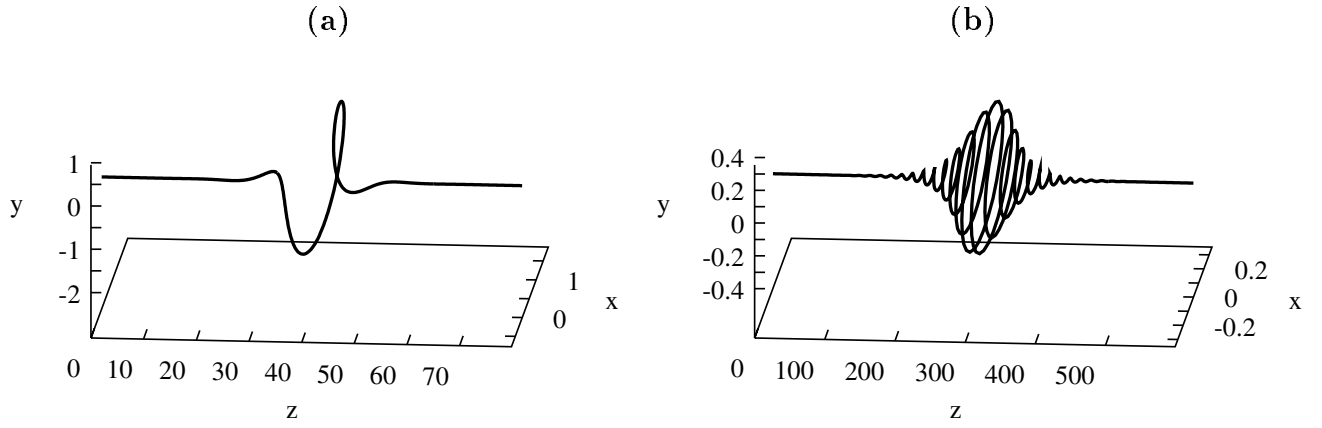\tag{31}
$$

10

Figure 1: The primary buckling mode at two different loads: (a) $m = 1.7$, (b) $m = 2.09$ ($\nu = \frac{1}{3}$, $\epsilon = 0.1$, $\gamma = 1$, implying $m_c = 2.097618$).

where $\mathcal{T}$ denotes the full length of the rod. Thus, $\tilde{D}$ and $\tilde{R}$ represent the true buckling contributions to end displacement and end rotation.

For comparison we have also included in Fig. 2 the deflections in the unperturbed case which can be computed exactly:

$$\tilde{D} = 2m\sqrt{4 - m^2}, \qquad\qquad \tilde{R} = 4 \arccos \frac{m}{2} \qquad\qquad (32)$$

(Thompson & Champneys 1996, Eqns. (5.3), (5.4)). We observe that shear causes an increase
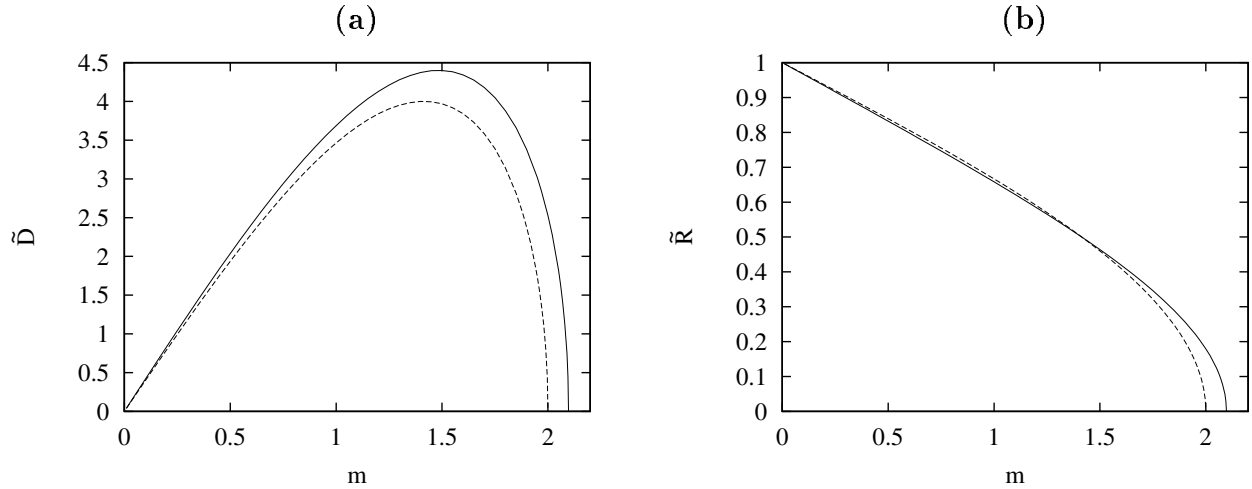
Figure 2: (a) End shortening $\tilde{D}$ and (b) end rotation $\tilde{R}$ versus load m for the primary homoclinic orbit ($\nu = \frac{1}{3}$, $\epsilon = 0.1$, $\gamma = 1$, implying $m_c = 2.097618$). Data for the unperturbed case has been included in dashed lines for comparison.

in the maximum end-shortening.

4 Initial curvature

Consider now a rod that is naturally curved, $\kappa_0 \neq 0$, while ignoring the effects of shear, gravity and non-symmetric cross-section, $\rho = \sigma = \epsilon = \delta = 0$.

4.1 One-twist-per-wave equilibria

Spatially-homogeneous equilibria of (13) $\boldsymbol{x}(t) \equiv \boldsymbol{x}^*$ are determined by setting the right hand sides of (13) to zero:

$$
\begin{align}
0 &= (1+\nu)x_2^* \, x_6^* - x_3^* \, x_5^* \tag{33}\\
0 &= x_3^* \, (x_4^* + \kappa_0) - (1+\nu) \, x_1^* \, x_6^* \tag{34}\\
0 &= x_1^* \, x_5^* - x_2^* \, (x_4^* + \kappa_0) \tag{35}\\
0 &= \nu x_5^* \, x_6^* + x_2^*/m^2 \tag{36}\\
0 &= (x_4^* + \kappa_0) \, x_6^* - (1+\nu)x_4^* \, x_6^* - x_1^*/m^2 \tag{37}\\
0 &= -\kappa_0 \, x_5^*. \tag{38}
\end{align}
$$

In addition, an equilibrium must satisfy the boundary constraints (15). From (38) we obtain $x_5^* = 0$ and hence from (36) that $x_2^* = 0$. Solving (34) and (37) for x_1^* and x_4^* in terms of x_3^* and x_6^* yields

$$
x_1^* = \frac{\kappa_0 \, m^2 \, (1+\nu) \, x_3^* x_6^*}{x_3^* + \, x_6^{*2} \, \nu(1+\nu) \, m^2} \qquad \text{and} \qquad x_4^* = \frac{\kappa_0[m^2 \, (1+\nu) \, x_6^{*2} - x_3^*]}{x_3^* + \, m^2\nu(1+\nu)x_6^{*2}}. \tag{39}
$$

Substitution into (39) of x_3^* and x_6^* from (15) (assuming them to be positive), leads to two coupled equations for x_1^* and x_4^*. A straightforward application of the Implicit Function Theorem shows that there is a unique solution for small κ_0 tending to $x_1^* = x_4^* = 0$ as $\kappa_0 \to 0$. This solution can be expressed as a series expansion for small κ_0:

$$
\begin{align}
x_1^* &= \frac{m^2 \, (1+\nu)}{\nu m^2(1+\nu)+1}\kappa_0 - \frac{m^2 \, (1+\nu)\left[m^2(1+\nu)\left(m^2 \, (2\nu^2+3\nu+1) - (\nu+2)\right)+1\right]}{2 \, \left(\nu m^2(1+\nu)+1\right)^4}\kappa_0^3 + \mathcal{O}(\kappa_0^5) \\[2mm]
x_2^* &= 0 \\[2mm]
x_3^* &= 1 - \frac{m^4 \, (1+\nu)^2}{2 \, \left(\nu m^2(1+\nu)+1\right)^2}\kappa_0^2 + \mathcal{O}(\kappa_0^4) \\[2mm]
x_4^* &= \frac{m^2(1+\nu)-1}{\nu m^2(1+\nu)+1}\kappa_0 - \frac{m^2 \, (1+\nu)^2 \, \left[m^4(1+\nu)^2 + 4m^2(1-\nu)+2\right]}{2 \, \left(\nu m^2(1+\nu)+1\right)^4}\kappa_0^3 + \mathcal{O}(\kappa_0^5) \tag{40}\\[2mm]
x_5^* &= 0 \\[2mm]
x_6^* &= 1 - \frac{\left(m^2(1+\nu)-1\right)^2}{2 \, \left(\nu m^2(1+\nu)+1\right)^2}\kappa_0^2 + \mathcal{O}(\kappa_0^4).
\end{align}
$$

Without using this expansion we shall now explicitly demonstrate that this equilibrium, when substituted into the Frenet-Serret and centre line differential equations (16), results in a

one-twist-per-wave solution. Now,

$$\tilde{\boldsymbol{u}} = (x_4^* + \kappa_0)\,\boldsymbol{d}_1 + (1 + \nu)x_6^*\,\boldsymbol{d}_3 =: J(\kappa_0, \nu, m)\,\boldsymbol{d}_1 + H(\kappa_0, \nu, m)\,\boldsymbol{d}_3, \tag{41}$$

where J and H are constants determined from the right-hand sides of (40). Hence equations (16) become

$$\dot{\boldsymbol{d}}_i = J(\boldsymbol{d}_1 \times \boldsymbol{d}_i) + H(\boldsymbol{d}_3 \times \boldsymbol{d}_i), \quad i = 1, 2, 3 \qquad \text{and} \qquad \dot{\boldsymbol{r}} = \boldsymbol{d}_3, \tag{42}$$

with the last equation arising because $\tilde{\boldsymbol{v}} = \boldsymbol{d}_3$ in the absence of shear. Note that for κ_0 small

$$J = \mathcal{O}(\kappa_0) \qquad \text{and} \qquad H = \mathcal{O}(1) \qquad \text{as} \qquad \kappa_0 \to 0. \tag{43}$$

The first three equations in (42) are

$$\dot{\boldsymbol{d}}_1 = H\boldsymbol{d}_2, \qquad \dot{\boldsymbol{d}}_2 = J\boldsymbol{d}_3 - H\boldsymbol{d}_1, \qquad \dot{\boldsymbol{d}}_3 = -J\boldsymbol{d}_2,$$

from which we can eliminate $\boldsymbol{d}_2$ to give

$$\begin{pmatrix} \ddot{\boldsymbol{d}}_1 \\ \ddot{\boldsymbol{d}}_3 \end{pmatrix} = \begin{bmatrix} -H^2 & HJ \\ HJ & -J^2 \end{bmatrix} \begin{pmatrix} \boldsymbol{d}_1 \\ \boldsymbol{d}_3 \end{pmatrix}. \tag{44}$$

Upon defining new orthonormal co-ordinate axes

$$\boldsymbol{e}_1 = \frac{1}{\sqrt{H^2 + J^2}}(H\boldsymbol{d}_1 - J\boldsymbol{d}_3), \quad \boldsymbol{e}_3 = \frac{1}{\sqrt{H^2 + J^2}}(J\boldsymbol{d}_1 + H\boldsymbol{d}_3), \quad \boldsymbol{e}_2 = \boldsymbol{e}_3 \times \boldsymbol{e}_1 = \boldsymbol{d}_2, \tag{45}$$

one finds from (44) that

$$\ddot{\boldsymbol{e}}_1 = -\Omega^2 \boldsymbol{e}_1 \qquad \text{and} \qquad \ddot{\boldsymbol{e}}_3 = 0, \tag{46}$$

where $\Omega = \sqrt{H^2 + J^2}$. The solution to these equations is

$$\boldsymbol{e}_1(t) = \boldsymbol{A}\cos\Omega t + \boldsymbol{B}\sin\Omega t, \qquad \boldsymbol{e}_3(t) = \boldsymbol{C}, \tag{47}$$

where $\boldsymbol{A}$, $\boldsymbol{B}$ and $\boldsymbol{C}$ are three constant orthonormal vectors determined by the initial conditions. Since there is no gravity, we are free to choose an origin for arclength and an orientation such that

$$\boldsymbol{A} = \boldsymbol{i}, \quad \boldsymbol{B} = \boldsymbol{j}, \quad \boldsymbol{C} = \boldsymbol{k}.$$

Note that the coefficient of t in the solution for $\boldsymbol{e}_3$ from (46) is chosen to be zero in order to avoid terms which grow as $t \to \pm\infty$. Inverting the transformation (45), we obtain an expression for the centre line of the rod via

$$\dot{\boldsymbol{r}} = \boldsymbol{d}_3 = \frac{1}{\Omega}(H\boldsymbol{e}_3 - J\boldsymbol{e}_1),$$

to give

$$\tilde{\boldsymbol{r}}(t) = \frac{H}{\Omega}\,t\,\boldsymbol{k} + \frac{J}{\Omega^2}(\cos\Omega t\,\boldsymbol{j} - \sin\Omega t\,\boldsymbol{i}). \tag{48}$$

Equation (48) describes a helix with amplitude J/Ω^2 and pitch angle $\frac{1}{2}\pi - \theta$, where $\theta = \arctan(J/H)$, the angle of rotation in the transformation (45). The central axis is directed
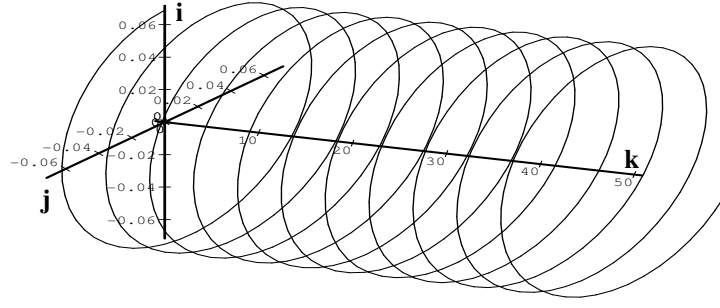
13

Figure 3: The dimensionless spatial configuration of the equilibrium solution (48) for $\nu = 1/3$, $\kappa_0 = 0.1$ and $m = 1$.

along $\boldsymbol{k}$ and the angular frequency Ω of the helix about its central axis is identical to that of the director $\boldsymbol{d}_1$, say, about that axis. *Hence (48) is a one-twist-per-wave spatially-homogeneous equilibrium configuration of the rod.*

Fig. 3 shows a solution (48) for some typical values of κ_0, m and ν, where H and J were determined by numerically solving the equations (39) and (15). Comparison with (24) gives that the dimensionless end-shortening per unit length is

$$\tilde{E} = 1 - \frac{H}{\Omega}.$$

Recall the relative sizes (43) of H and J for small κ_0. Hence note that $\tilde{E} \to 0$ as $\kappa_0 \to 0$, as does the amplitude of the helix J/Ω^2. Fig. 4 shows how the amplitude and end-shortening vary with m and κ_0.

4.2 Linearisation

Linearisation around the equilibrium $\boldsymbol{x}^*$ shows that (13) always has two zero eigenvalues, as in the unperturbed case, which correspond to the rotational symmetry in the problem. The other four eigenvalues satisfy the characteristic equation

$$
\begin{aligned}
\lambda^4 &+ \left(-2\,x_3^*\,m^2 + \frac{5\,m^4\kappa_0 x_4^*}{3} + \frac{17\,m^4 x_6^{*2}}{9} + 2m^4\kappa_0^2 + m^4 x_4^{*2} \right) \lambda^2 m^{-4} \\
&+ \left(-m^2 x_3^*\,x_4^{*2} - \frac{10\,m^4 x_6^{*2}\kappa_0 x_4^*}{27} + \frac{16\,m^4 x_6^{*4}}{81} + \frac{8\,x_6^{*2}m^2 x_3^*}{9} + x_3^{*2} \right. \\
&+ \frac{5\,x_6^*\,m^2 x_4^*\,x_1^*}{3} + \frac{35\,x_6^*\,m^2\kappa_0 x_1^*}{9} - 2m^2 x_3^*\,\kappa_0^2 - \frac{m^4\,x_4^{*3}\,\kappa_0}{3} + \frac{m^4\,x_4^{*2}\,\kappa_0^2}{3} \\
&+ \frac{17\,m^4 x_6^{*2}\kappa_0^2}{9} + m^4\,\kappa_0^4 + \frac{5\,m^4\,x_4^*\,\kappa_0^3}{3} + \frac{m^4 x_6^{*2} x_4^{*2}}{9} - \left. \frac{5\,m^2 x_3^*\,\kappa_0 x_4^*}{3} \right) m^{-4} = 0, \quad (49)
\end{aligned}
$$

where, for simplicity, it is assumed that Poisson's ratio takes the numerical value $\nu = 1/3$. This value will be taken in all numerical simulations which follow.
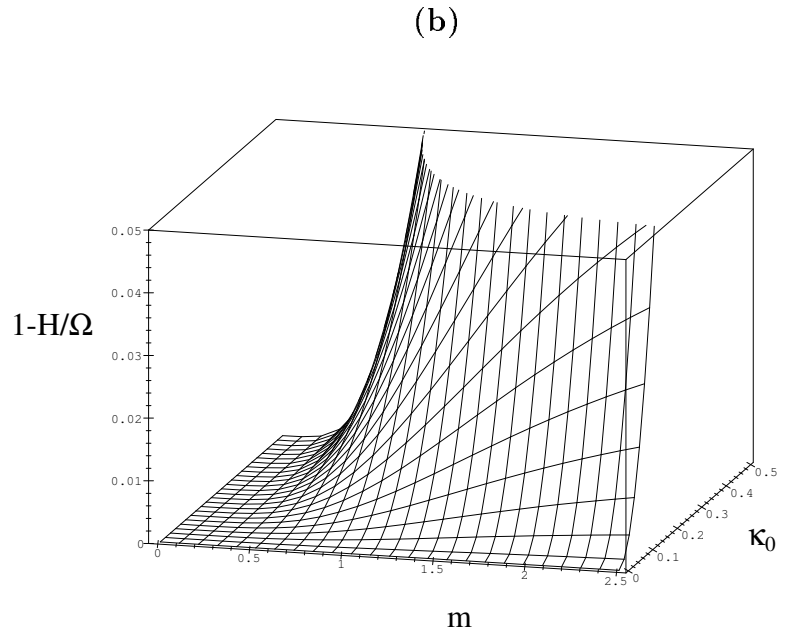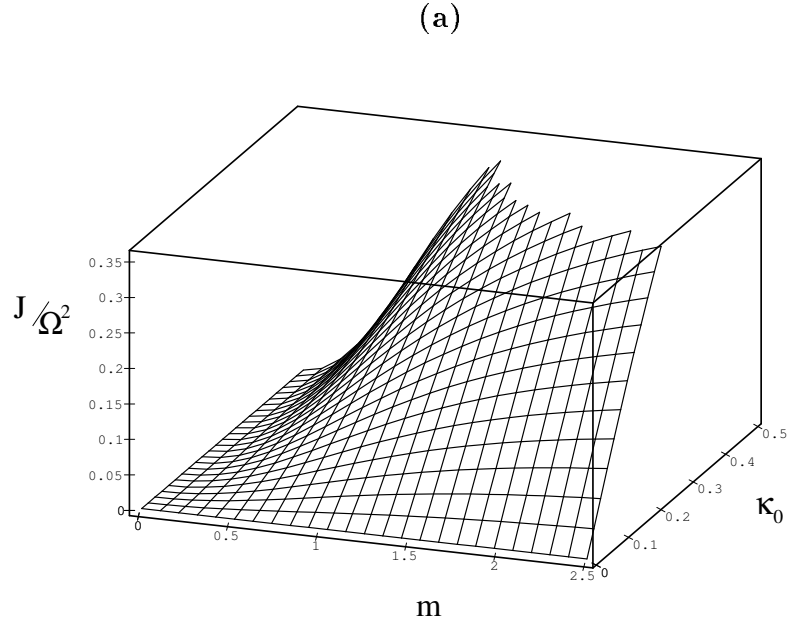
$$\mathbf{J}\big/\Omega^2$$

$$1\text{-}\mathrm{H}/\Omega$$

Figure 4: Three-dimensional plots of the amplitude (a) and end-shortening (b) of the helix (48) for $\nu = 1/3$, $0 \leq \kappa_0 \leq 0.5$ and $0 < m \leq 2.5$.
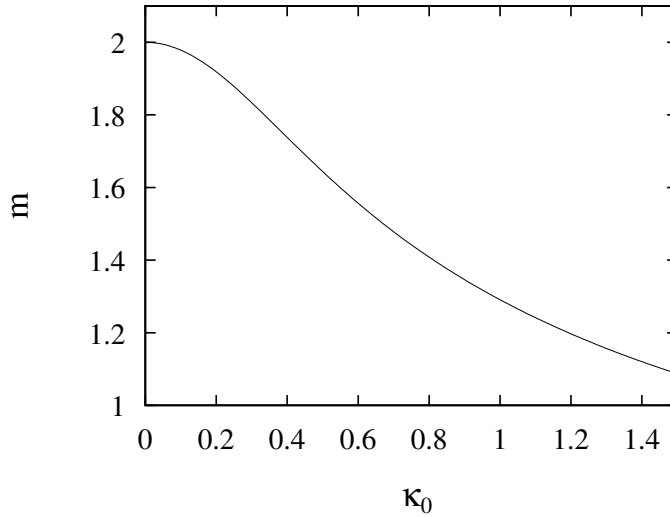
Figure 5: Locus in the (m, κ_0)-plane of Hamiltonian-Hopf bifurcation points.

Analysis of (49) using Maple (solving for x_1, x_3, x_4 and x_6 using (39) and (15)) reveals that the situation is qualitatively the same as the unperturbed case with $\rho = 0$, $\kappa_0 = 0$. Namely that for $m < m_c(\kappa_0)$ there are four complex eigenvalues $\pm\lambda \pm i\,\omega$, implying physical stability of the spatially-homogeneous equilibrium, and that at $m = m_c$ there is a Hamiltonian-Hopf bifurcation, with physical instability (four imaginary eigenvalues) occurring for $m > m_c$. A plot of $m_c(\kappa_0)$ is given in Fig. 5, which was determined numerically by solving for double roots of (49). Note that the value of m required for the buckling bifurcation to occur is initially flat and then decreases with increasing initial curvature κ_0.

4.3   Localised buckling solutions

First note that adding initial curvature destroys part of the symmetry of the unperturbed system. Specifically, of the two symmetries R_1 and R_2 only R_2 remains (R_1 would have remained had we taken initial curvature about $\boldsymbol{d}_2$ instead of $\boldsymbol{d}_1$). Consequently, we should expect the existence of two rather than four reversible primary buckling modes. Our shooting method indeed gives us the two homoclinic orbits shown in Fig. 6. These solutions were computed for $\nu = \frac{1}{3}$, $\kappa_0 = 0.02$ and $m = 1.7$, while in the shooting method we used $\epsilon = 10^{-5}$ and

$$\boldsymbol{v}_1 = (0.582029 \times 10^{-4},\ 0.609510,\ -0.196407 \times 10^{-5},\ 0.188564,\ 0.304719,\ -0.00636259),$$
$$\boldsymbol{v}_2 = (-0.609205,\ 0,\ 0.0205577,\ -0.304777,\ 0.188629,\ 0.00494804).$$

See van der Heijden et al. (1996) for the meaning of ϵ, δ and $\boldsymbol{v}_i$.

Three-dimensional rod shapes, obtained by solving the centre line equation in (16), are depicted in Fig. 7. The figure nicely shows the small-amplitude helical solution of the rod away from the large deformation. Fig. 8 shows one primary mode for large initial curvature $\kappa_0 = 0.4$. Here the distinction between the pre-buckled one-twist-per-wave equilibrium and the large deformation is somewhat blurred.

Because asymptotically towards infinity the spatially-homogeneous solution is a helical rather than a straight rod, the $\boldsymbol{d}_3$ director of the local co-ordinate frames at the beginning
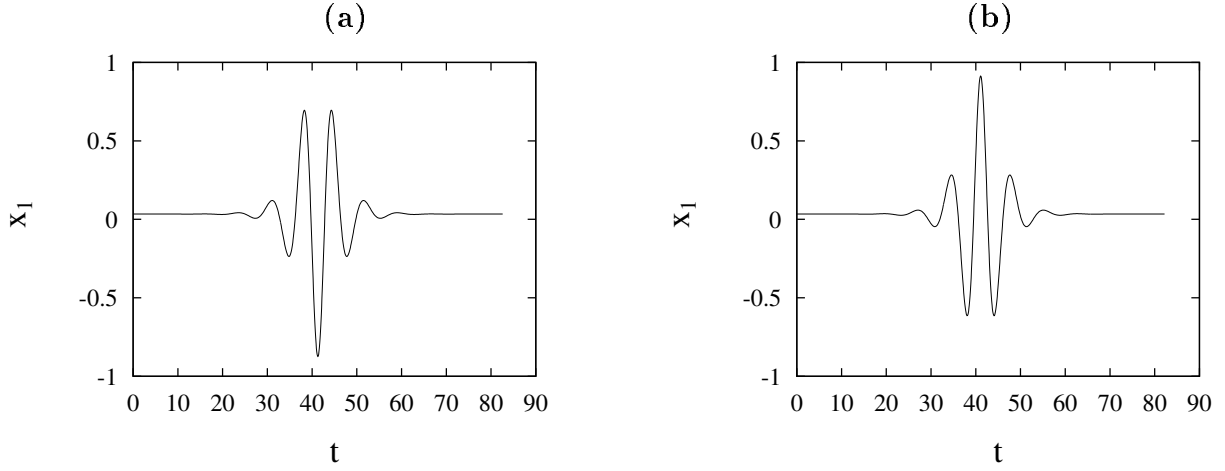
16

Figure 6: The two R_2-reversible primary buckling modes: (a) P_1 ($\delta = 5.156917$, $\mathcal{T} = 41.299427$); (b) P_2 ($\delta = 1.807504$, $\mathcal{T} = 41.097204$). ($\nu = \frac{1}{3}$, $\kappa_0 = 0.02$, $m = 1.7$.)
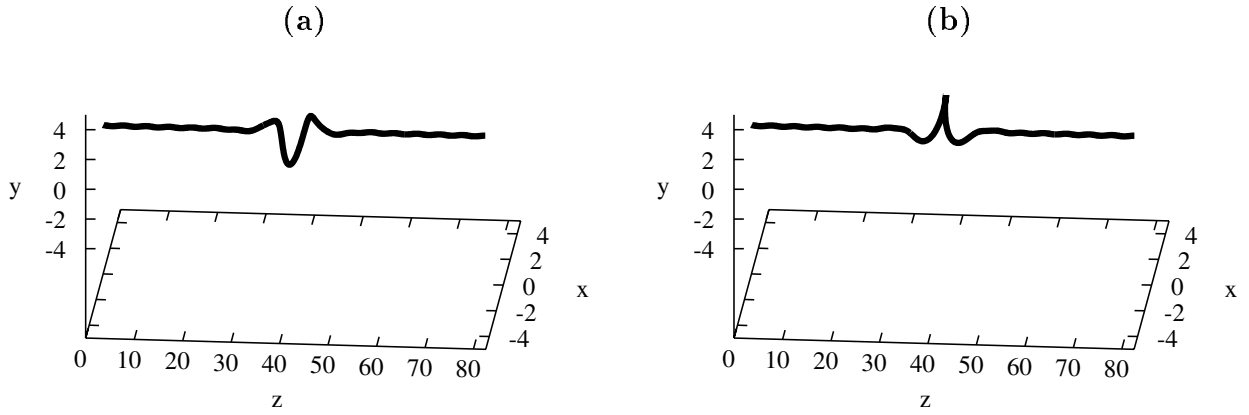

Figure 7: The two primary buckling modes P_1 (a) and P_2 (b) ($\nu = \frac{1}{3}$, $\kappa_0 = 0.02$, $m = 1.7$).
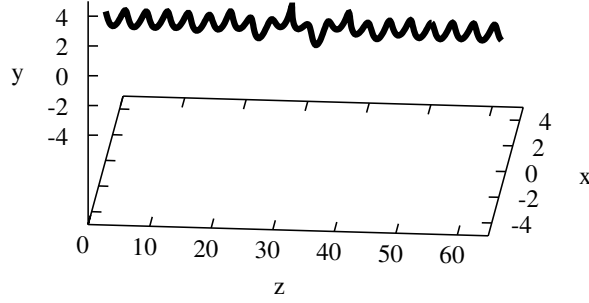
Figure 8: The primary buckling mode P_1 for large initial curvature ($\nu = \frac{1}{3}$, $\kappa_0 = 0.4$, $m = 1.7$).

and end point do not line up. We can, therefore, not use (27) directly to obtain the end deflections. End shortening and end rotation are now naturally computed with respect to the central axis $\boldsymbol{e}_3 = \boldsymbol{k}$ of the helix. Thus, to get the end rotation we determine the projections $\hat{\boldsymbol{d}}_1$, $\hat{\boldsymbol{d}}_2$ of the vectors $\boldsymbol{d}_1$, $\boldsymbol{d}_2$ of the local co-ordinate frames at both ends of the rod onto the plane $(\boldsymbol{e}_1, \boldsymbol{e}_2)$ orthogonal to the axis $\boldsymbol{k}$. D and R are then computed from:

$$D = \mathcal{T} - \boldsymbol{e}_3(\mathcal{T}), \quad \cos R = <\hat{\boldsymbol{d}}_1(\mathcal{T}), \hat{\boldsymbol{d}}_1(0)>, \quad \sin R = <\hat{\boldsymbol{d}}_1(\mathcal{T}), \hat{\boldsymbol{d}}_2(0)>, \qquad (50)$$

where $\mathcal{T}$ represents the full length of the rod. Note that, in view of (45), $\hat{\boldsymbol{d}}_2 = \boldsymbol{d}_2$, and hence $\hat{\boldsymbol{d}}_2(0) = (0, 1, 0)$. The clean buckling contributions to the end deflections are again obtained from D and R by subtracting the contributions from the trivial solution, this time a helix:

$$\tilde{D} = (1 - \tilde{E}) \, \mathcal{T} - \boldsymbol{e}_3(\mathcal{T}), \qquad \tilde{R} = \frac{R - \Omega \, \mathcal{T}}{2\pi}. \qquad (51)$$

Load-deflection diagrams are given in Fig. 9. Fig. 10 shows how end shortening and end rotation change as the initial curvature κ_0 is varied. Note that the diagram of Fig. 10 is symmetric about $\kappa_0 = 0$ (with a change of role of P_1 and P_2), as expected. At $\kappa_0 = 0$ the symmetric modes P_1 and P_2 are part of a full circle of primary homoclinic orbits, all with the same load-deflection characteristics. Indeed, the corresponding $\tilde{D}$ and $\tilde{R}$ values are those of the unperturbed case included in dashed lines in Fig. 2.

The continuation code with fixed $\mathcal{T} = 82.5$ (full-length rod) has problems in the steep regions close to buckling, which is why the load-deflection curves do not reach right down to the κ_0-axis. A numerical check with larger values of the truncation interval $\mathcal{T}$ shows that the curves can be followed further down as $\mathcal{T}$ is increased. Hence, we conclude that we are dealing with an effect due to finite $\mathcal{T}$ and that P_1 and P_2 really bifurcate from the trivial solution at $\kappa_0 = 0.439763$.

Apart from breaking the symmetry of the unperturbed system, initial curvature also breaks complete integrability. Specifically, we no longer have conservation of torque about the body axis of the rod, i.e., $I_3 \neq$ const. As a result, we have a situation analogous to the case of an
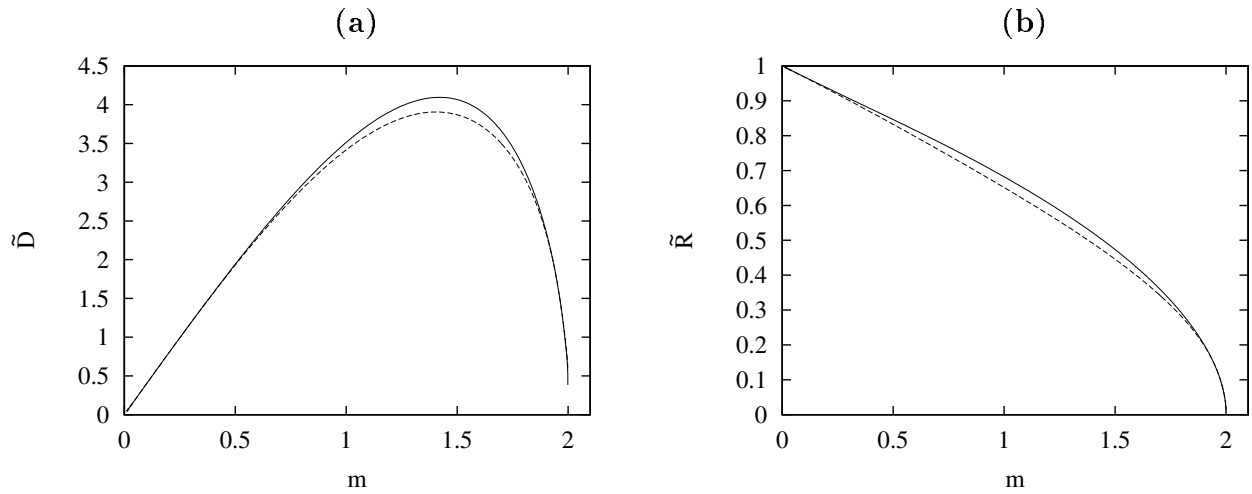
18

Figure 9: (a) End shortening $\tilde{D}$ and (b) end rotation $\tilde{R}$ versus load m for the primary homoclinic orbits P_1 (solid curves) and P_2 (dashed curves) ($\nu = \frac{1}{3}$, $\kappa_0 = 0.02$, implying $m_c = 1.999116$).

anisotropic rod studied extensively in van der Heijden et al. (1996), with a countable infinity of multi-modal homoclinic orbits amidst spatial chaos. These multi-modal solutions are located in the transverse intersection of the invariant manifolds of the fixed point and roughly consist of multiple copies of primary solutions separated by finite numbers of small-amplitude oscillations.

Table 1 gives data for the first fifteen members of two families of R_2-reversible bi-modals. The homoclinic orbits of one family are built up of two P_1-type humps and are accordingly
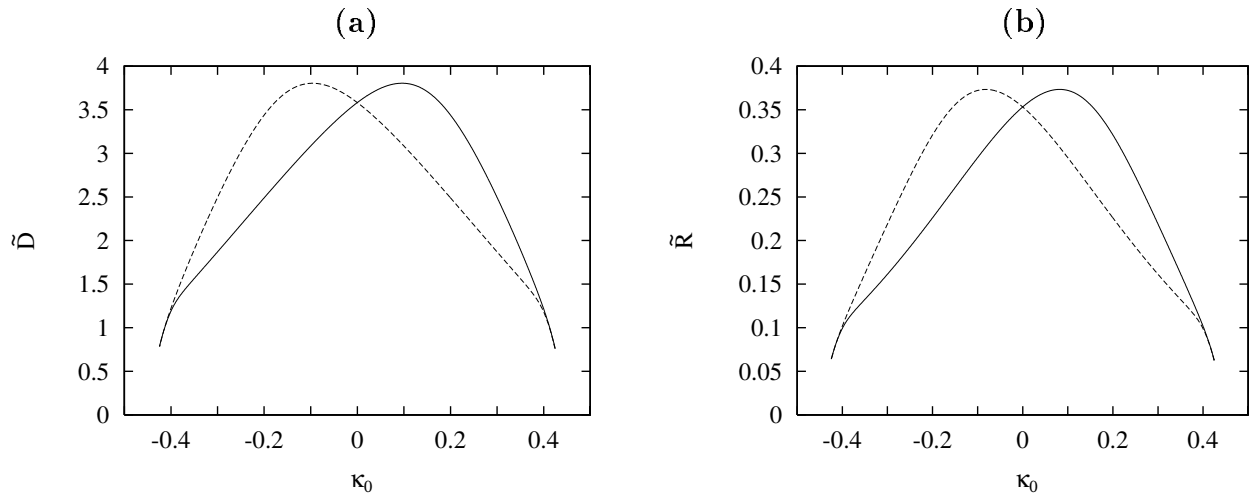

Figure 10: (a) End shortening $\tilde{D}$ and (b) end rotation $\tilde{R}$ versus initial curvature κ_0 for the primary homoclinic orbits P_1 (solid curves) and P_2 (dashed curves) ($\nu = \frac{1}{3}$, $m = 1.7$, implying the critical buckling value $\kappa_0 = 0.439763$).

19

labelled (P_1, n, P_1), where n is a measure of the number of small oscillations between the two large deformations (the choice of origin for n is somewhat arbitrary). Similarly, the orbits of the other family look like two copies of P_2 and are labelled (P_2, n, P_2). Data for $(P_2, 2, P_2)$ is missing because this orbit could not be found. It is not clear whether this solution somehow does not exist for the parameters used, or that our shooting method just failed to locate it. As to the former possibility, coalescence rules for multi-modal orbits as derived (for the non-symmetric case) in van der Heijden et al. (1996) might give some clarification.

Note that for both families the δ-values converge to that of the corresponding primary orbit, while the difference between successive $\mathcal{T}$-values tends to $\frac{\pi}{2\omega}$, where ω is the (positive) imaginary part of the complex quadruple of eigenvalues at the fixed point $\boldsymbol{x}^*$. This limiting behaviour can be understood by imagining, in phase space, each successive homoclinic orbit in the sequence making an extra quarter turn around the fixed point immediately prior to hitting the symmetric section. Fig. 11(a) and (b) show x_1-t plots for one member of each of the above two families of bi-modals.

The two infinite families (P_1, n, P_1) and (P_2, n, P_2) define all bi-modals which are themselves reversible. Non-reversible bi-modals with labels (P_1, n, P_2) and (P_2, n, P_1) do exist but are not captured by our shooting method in the present form. Two examples of non-reversible bi-modals, obtained by shooting over the full length of the rod, are given in Fig. 11(c) and (d). As in the case of an anisotropic rod, reversible tri-modals, four-modals and higher-order multi-modals occur in similar families parametrised by multiple integers.

We should stress that our boundary conditions ensure that all the homoclinic orbits are computed for the same values of the two integrals of motion I_1 and I_2, namely those of the

n	δ_n	$\mathcal{T}_n$	$\mathcal{T}_n - \mathcal{T}_{n-1}$		n	δ_n	$\mathcal{T}_n$	$\mathcal{T}_n - \mathcal{T}_{n-1}$
1	5.527777	52.129804			1	2.520175	50.544884	
2	5.008232	53.422228	1.292424		2			
3	5.199237	55.519861	2.097633		3	1.913620	53.569436	
4	5.143442	57.342668	1.822808		4	1.769202	55.268184	1.698748
5	5.161089	59.246022	1.903353		5	1.818802	57.217025	1.948841
6	5.155616	61.124430	1.878408		6	1.803924	59.081629	1.864604
7	5.157323	63.010459	1.886029		7	1.808612	60.972140	1.890511
8	5.156791	64.894152	1.883693		8	1.807158	62.854410	1.882270
9	5.156957	66.778561	1.884408		9	1.807611	64.739273	1.884863
10	5.156905	68.662750	1.884189		10	1.807470	66.623317	1.884044
11	5.156921	70.547006	1.884256		11	1.807514	68.507620	1.884303
12	5.156916	72.431244	1.884237		12	1.807500	70.391841	1.884221
13	5.156918	74.315485	1.884241		13	1.807505	72.276088	1.884247
14	5.156917	76.199725	1.884240		14	1.807503	74.160327	1.884239
15	5.156917	78.083965	1.884240		15	1.807504	76.044568	1.884241
P_1	5.156917	41.299427	$\frac{\pi}{2\omega} = 1.884241$		P_2	1.807504	41.097204	$\frac{\pi}{2\omega} = 1.884241$

Table 1: Sequence of R_2-reversible bi-modal homoclinic orbits with labels (P_1, n, P_1) (left) and (P_2, n, P_2) (right) for rods with initial curvature ($\nu = \frac{1}{3}$, $m = 1.7$, $\kappa_0 = 0.02$).
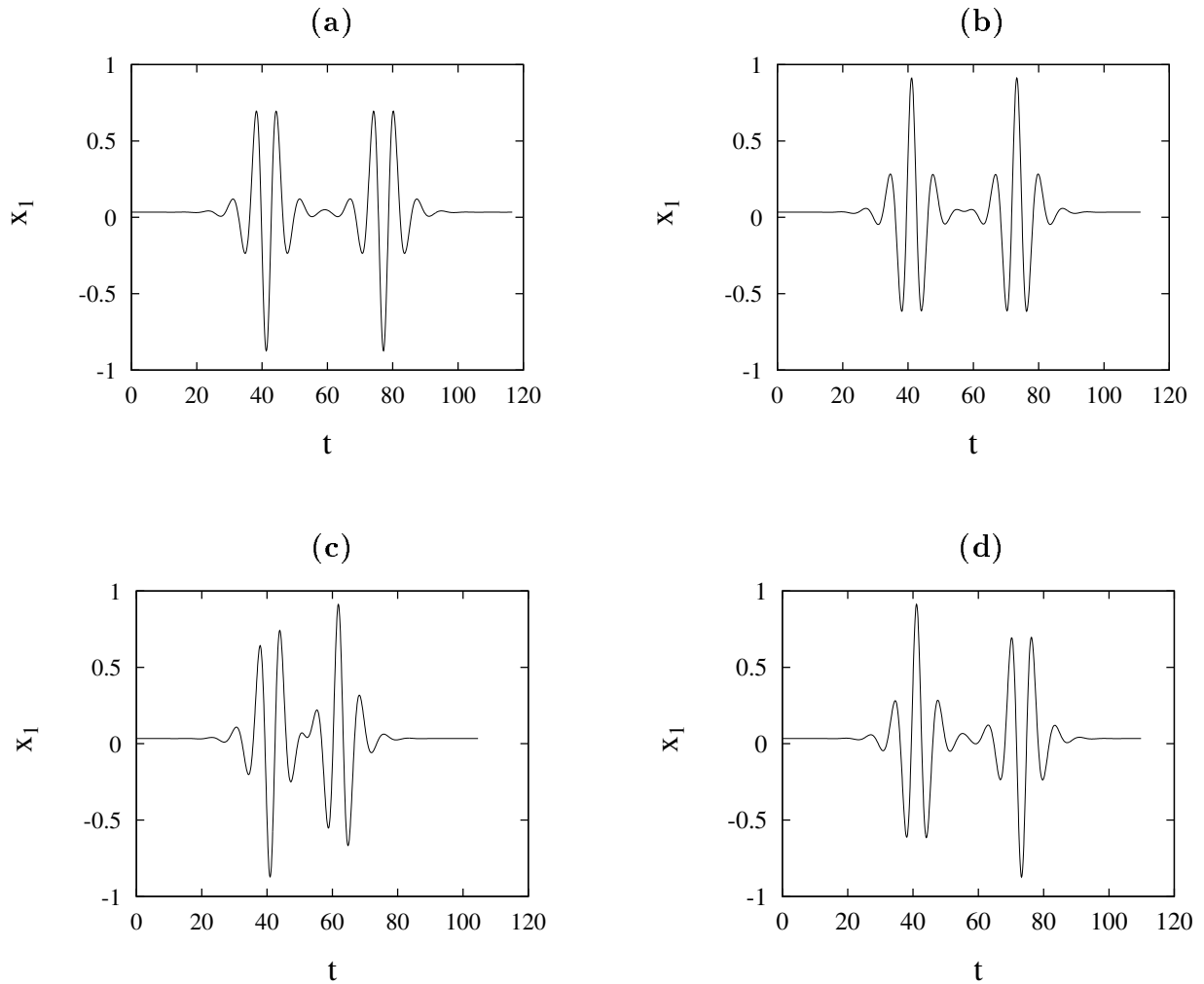
Figure 11: Two examples of R_2-reversible bi-modal homoclinic orbits: (a) orbit $(P_1, 5, P_1)$, (b) orbit $(P_2, 5, P_2)$. Two examples of non-reversible bi-modal homoclinic orbits: (c) $\delta = 4.768824$, length $= 104.618967$, (d) $\delta = 1.795082$, length $= 109.838808$ ($\nu = \frac{1}{3}$, $\kappa_0 = 0.02$, $m = 1.7$).

one-twist-per-wave equilibrium to which the localised solutions asymptote as $t \to \pm\infty$.

5 Physical interpretation

Let us finally make some physical interpretations of the results obtained. The main achievement of this paper is to demonstrate that a uniform initial curvature in the stress-free state does indeed give rise to one-twist-per-wave equilibria upon which localised buckling is superimposed at the critical load. Note from Fig. 5 that the critical buckling condition is not changed much by the introduction of small initial curvature. Neither is the post-buckling path of the primary buckling mode (compare Figs. 9 and 2).

We have also shown that (at least for the initially straight rod) allowing for shear/axial

deformations makes little qualitative difference. However, when interpreting experiments under rigid loading it is important to note that 'shear' deformations, specifically axial extension, must occur if the rod is seen to buckle into a non-straight configuration. We must also take care not to make glib statements on experiments based on the so-far *dimensionless* analysis.

Note from the non-dimensionalisation (12) that both $\tilde{r}$ and t scale with M/B. Recalling that we are assuming a symmetric cross-section (i.e., $A = B$), the equilibrium solution (48) can then be written in dimensional co-ordinates as

$$r(s) = \frac{H}{\Omega} s\,k + \frac{AJ}{M\Omega^2}(\cos\omega s\,j - \sin\omega s\,i), \qquad \text{where} \qquad \omega = \frac{M\Omega}{A}. \tag{52}$$

From (12), (40) and (41) it follows that for small initial curvature u_0 the dimensional helical characteristics are given by

$$\begin{aligned}
\text{radius} &= \frac{AJ}{M\Omega^2} = \frac{AC^2}{M^2(A-C)+TC^2}\,u_0 + \mathcal{O}\left(u_0^3\right), \\
\text{frequency} &= \omega = \frac{M}{A}\Omega = \frac{M}{A}(1+\nu) + \mathcal{O}\left(u_0^2\right) = \frac{M}{C} + \mathcal{O}\left(u_0^2\right), \\
\tfrac{1}{2}\pi - \text{pitch angle} &= \theta = \arctan\left(\frac{J}{H}\right) = \frac{ACM}{M^2(A-C)+TC^2}\,u_0 + \mathcal{O}\left(u_0^3\right).
\end{aligned} \tag{53}$$

We have explicitly computed the one-twist-per-wave helical equilibrium for the case where initial curvature is the only perturbation allowed in Fig. 13. It is easy to see, however, that the whole analysis goes through when anisotropy (ρ) and shear/extension (ϵ) are also taken into account. The crucial observation is that in the more general case we still have

$$x_2^* = x_5^* = 0. \tag{54}$$

Hence, although Ω will vary with ρ and ϵ we will still have a one-twist-per-wave solution. Note that (54) means that along the rod there is no force or moment in the direction d_2; the helical rod is bent in the direction d_1 of initial curvature, and forces and moments are in the tangent plane to the imaginary cylinder on which the helix winds. Indeed, it can be verified that the force, n, is directed along the axis of the helix. The moment, m, however, is not. In experiments one is likely to control the axial moment, $M_{\mathrm{ax}} := m \cdot e_3$, rather than the total moment M. In the Appendix, therefore, an analysis is given in terms of the axial moment. To first order in κ_0 (or u_0) taking M_{ax} or M does not make any difference: (53) is also valid with M replaced by M_{ax}.

If, in addition to initial curvature u_0, we also take M to be small, but such that $\kappa_0 = Au_0/M$ remains small (for instance by taking $u_0 = \mathcal{O}(\epsilon)$, $M = \mathcal{O}(\sqrt{\epsilon})$, in terms of an arbitrary small parameter ϵ), then to a good approximation (53) can be written as:

$$\text{radius} = \frac{Au_0}{T}, \qquad \text{frequency} = \frac{M}{C}, \qquad \tfrac{1}{2}\pi - \text{pitch angle} = \frac{AMu_0}{TC}, \tag{55}$$

which is in agreement with the approximations (60) given in the Appendix.

We end by discussing some experiments serving to confirm the central result of this paper. The one-twist-per-wave pre-buckling deformations observed experimentally by Thompson & Champneys (1996) are shown in Fig. 12 for a circular rubber rod. Moving down through the

22

(Photograph 1)

Figure 12: A photographic sequence during the test of an initially curved rod of circular cross-section. A one-twist-per-wave helical deformation is observed before the localised buckling.

(Photograph 2)

Figure 13: A photographic sequence during the under-water test of a silicone rubber rod of square cross-section. The rod had no initial curvature, and only a straight trivial state is observed before the localised buckling.

sequence of pictures, as the loading is increased, we see a large-amplitude localised buckling mode with about 3 twists per wave superimposed on top of this pre-buckling response. The significance of the 3 is that it is approximately $2(1 + \nu)$, as ν, Poisson's ratio of rubber, is approximately 0.5. This rod certainly had an initial curvature in its unstressed state, and the work of the present paper suggests very strongly indeed that this curvature was the cause of the one-twist-per-wave behaviour.

This conclusion is reinforced by the more recent experiments illustrated in Fig. 13 for a rod of square cross-section. This highly perfect rod, with no measurable initial curvature, was cast in silicone rubber. It was kindly supplied by C.R. Calladine of the Cambridge Engineering Laboratory. It was tested under water, under conditions of approximately neutral buoyancy. No pre-buckling deformation is observed, and the localised buckling mode, with about 3 twists per wave, arises directly from the trivial highly-twisted straight configuration. Under the rigid loading of the test, a dynamic jump at constant end-shortening and constant end-rotation carries the rod from a buckled configuration (like that shown in the third picture) to self-contact in the writhing configuration of the fourth picture. The bottom picture shows the freely floating straight rod after the test. The high quality silicone rubber shows no sign of having suffered any permanent deformation during the test.

A Appendix: Physical analysis of one-twist-per-wave equilibria

It is instructive to make a direct physical study of the possible one-twist-per-wave equilibrium solutions of twisted rods. Consider a rod with principal bending stiffnesses A and B, which may or may not be equal, and torsional stiffness C. Let the rod have an initial curvature κ_0, which may or may not be zero, in the principal direction associated with A. We use as a measure of this curvature the applied bending moment that would just straighten the rod,

23

(Picture of one-twist-per-wave helix)

Figure 14: A helical equilibrium state with one twist per wave, showing the resultant forces and moments at a cross-section of the rod. These are statically equivalent to a wrench (M_{ax}, T) acting along the central chain-dotted axis.

namely $N = A\kappa_0$.

Inducing only (additional) bending in the A direction, consider a helical deformation in which the rod is wrapped with one twist per helical wave around an imaginary cylinder of radius r. Since there is no bending in the B direction, it follows that B will not appear in our analysis: it may or may not be equal to A. The assumed helical form is illustrated in Fig. 14 for a rod with a square cross-section. Here it should be supposed that in its unloaded state the initial curvature was such that the rod lay in a circle with the outer edge black.

Cutting the homogeneous helix at any point, the resultant moment vector, M, is the resultant of the bending moment $A(\kappa - \kappa_0)$ and the twisting moment $C\tau$, as illustrated. The bending moment is at right angles to the rod, the twisting moment is along the rod, and all three vectors lie in the tangent plane of the cylinder. Here, κ is the curvature of the helical space curve, given by the standard formula $\kappa = \sin^2\theta/r$, where $\frac{1}{2}\pi - \theta$ is the pitch angle of the helix. With one twist per wave there is no internal twist ($\tau_i = 0$), so the twist, τ, is equal to the torsion of the helical space curve, $\tau = \tau_s = \sin\theta\cos\theta/r$.

For a homogeneous solution, the resultant force at the cut must be parallel to the axis, and we denote its magnitude by T. For the purpose of overall statics, we can transfer the line of action of T to the central axis of the cylinder with the introduction of the transfer moment of magnitude Tr lying in the tangent plane. Now the constant support reactions supplied at the remote left-hand end of the helix must be in balance with the above forces and moments at whatever phase, within a wave, the helix is cut. This is only possible if the vector sum of M and the transfer moment is parallel to the axis of the cylinder; notice that the vector of magnitude Tr drawn in the figure is the reversed transfer moment.

Under these conditions the helix is held in equilibrium by a wrench (compare Love (1927, art. 270)) comprising the axial tension, T, and the axial moment, M_{ax}. Notice that M_{ax} is the axial component of the resultant moment M considered in the main body of this paper.

Setting the axial and circumferential components of M equal to M_{ax} and Tr, respectively, we have

$$M_{\text{ax}} = C\tau\cos\theta + (A/r)\sin^3\theta - N\sin\theta,$$
$$Tr = C\tau\sin\theta - (A/r)\sin^2\theta\cos\theta + N\cos\theta. \tag{56}$$

24

Applying the one-twist-per-wave requirement, $\tau = \tau_s = \sin\theta \cos\theta / r$, gives

$$M_{\mathrm{ax}} = (C/r)\sin\theta\cos^2\theta + (A/r)\sin^3\theta - N\sin\theta,$$
$$Tr = (C/r)\sin^2\theta\cos\theta - (A/r)\sin^2\theta\cos\theta + N\cos\theta. \qquad (57)$$

Prescribing N, M_{ax} and T, these are two equations for the two helical variables θ and r. A first-order solution valid for small θ is given by

$$M_{\mathrm{ax}}/\theta = C/r - N, \qquad (58)$$
$$Tr = (C - A)\theta^2/r + N. \qquad (59)$$

Bending solution for the initially curved rod ($N \neq 0$)
Let us suppose that under a fixed T we gradually increase M_{ax} from zero. With $M_{\mathrm{ax}} = 0$ we have the trivial physical solution with $\theta = 0$, $Tr = N$. This satisfies (59), and leaves (58) indeterminate. A first-order solution close to this trivial state, valid for small N, is given by

$$\theta = \frac{M_{\mathrm{ax}}N}{CT}, \qquad\qquad r = \frac{N}{T}. \qquad (60)$$

So to first order, for fixed T and N, the radius r is a constant, while the angle θ increases linearly with M_{ax}.

Buckling solution for a perfect ($N = 0$) anisotropic rod
We next focus on the perfect ($N = 0$) rod with unequal principal bending stiffnesses. For such an anisotropic rod we would expect the one-twist-per-wave, tape-like behaviour to involve bending about the weak axis. So we are led to assume $B > A$.

For a perfect rod, with $N = 0$, equation (58) gives

$$\frac{\theta}{r} = \frac{M_{\mathrm{ax}}}{C} \qquad (61)$$

and substituting into (59) gives

$$\frac{M_{\mathrm{ax}}^2}{T} = \frac{C^2}{C - A}. \qquad (62)$$

Now the perfect rod (with fixed T, say) has the trivial solution $\theta = r = 0$, valid for all $M_{\mathrm{ax}}(= M)$. We can therefore identify (61), (62) (valid as $\theta \to 0$) as an eigenvalue problem with a non-trivial solution determined by the critical value of M_{ax}. Thus, (62) gives the critical buckling condition.

We see that for a real buckling solution we need C greater than the relevant bending stiffness (here, A). For a solid section, C is usually of the order of the lesser bending stiffness. So this analysis shows that there will usually be no possible equilibrium state for a tape-like rod standing, rather than lying, on the imaginary cylinder, a result also reached in van der Heijden & Thompson (1996).

The dimensionless version of (62), using (12), reads

$$m^2 = \frac{1 + \rho}{(1 + \nu)(\rho - \nu)}. \qquad (63)$$

This is the equation for the curve m_{c_3} in the ρ-m parameter planes in Champneys & Thompson (1996) and van der Heijden et al. (1996). It is shown in van der Heijden & Thompson (1996) that under some conditions this curve is part of the buckling line, describing (lying) tape-like buckling.

References

Antman, S. (1995), *Nonlinear Problems of Elasticity*, Springer-Verlag, Berlin. Apllied Mathematical Sciences 107.

Antman, S. & Jordan, K. (1974), 'Qualitative aspects of the spatial deformation of non-linearly elastic rods', *Proc. Roy. Soc. Edin. A* **73**, 85–105.

Champneys, A. & Spence, A. (1993), 'Hunting for homoclinic orbits in reversible systems: a shooting technique', *Adv. Comp. Math.* **1**, 81–108.

Champneys, A. & Thompson, J. (1996), 'A multiplicity of localised buckling modes for twisted rod equations', *Proc. Roy. Soc. Lond. A* **452**, 2467–2491.

Doedel, E., Keller, H. & Kernévez, J. (1991), 'Numerical analysis and control of bifurcation problems: (I) Bifurcation in finite dimensions', *Int. J. Bifurcation and Chaos* **1**, 493–520, 745–772.

Iooss, G. & Pérouème, M. (1993), 'Perturbed homoclinic solutions in reversible 1:1 resonance vector fields', *J. Diff. Eq.* **102**, 62–88.

Kehrbaum, S. & Maddocks, J. (1997), 'Elastic rods, rigid bodies, quaternions and the last quadrature'. This issue of *Phil. Trans. R. Soc. Lond. A*.

Kirchhoff, G. (1859), 'Über das Gleichgewicht und die Bewegung eines unendlich dünnen elastischen Stabes', *J. für Mathematik (Crelle)* **56**, 285–313.

Love, A. (1927), *A Treatise on the Mathematical Theory of Elasticity*, 4th ed. edn, Cambridge University Press, Cambridge.

Mielke, A. & Holmes, P. (1988), 'Spatially complex equilibria of buckled rods', *Arch. Rat. Mech. Anal.* **101**, 319–348.

Thompson, J. & Champneys, A. (1996), 'From the helix to localized writhing in the torsional post buckling of elastic rods', *Proc. R. Soc. Lond.* **452**, 117–138.

Timoshenko, S. & Gere, J. (1961), *Theory of elastic stability*, McGraw-Hill, New York.

van der Heijden, G. & Thompson, J. (1996), 'Lock-on to tape-like behaviour in the torsional buckling of anisotropic rods'. Report, Centre for Nonlinear Dynamics, University College London.

van der Heijden, G., Champneys, A. & Thompson, J. (1996), 'Load-deflection characteristics of localised torsional buckling modes in rods with non-circular cross-section'. Submitted to *SIAM J. Appl. Math.*

van der Meer, J. (1985), *The Hamiltonian Hopf bifurcation (Lecture Notes in Mathematics 1160)*, Springer-Verlag, Berlin.